Nine Localized Deviations from Keplerian Rotation in the DSHARP Circumstellar Disks: Kinematic Evidence for Protoplanets Carving the Gaps

C. Pinte[1,2] , D. J. Price[1] , F. Ménard[2] , G. Duchêne[2,3] , V. Christiaens[1] , S. M. Andrews[4] , J. Huang[4] , T. Hill[5] ,
G. van der Plas[2] , L. M. Perez[6] , A. Isella[7] , Y. Boehler[2] , W. R. F. Dent[5] , D. Mentiplay[1] , and R. A. Loomis[8]

[1] School of Physics and Astronomy, Monash University, Clayton, Vic 3800, Australia; christophe.pinte@monash.edu
[2] Univ. Grenoble Alpes, CNRS, IPAG, F-38000 Grenoble, France
[3] Astronomy Department, University of California, Berkeley, CA 94720-3411, USA
[4] Harvard-Smithsonian Center for Astrophysics, 60 Garden Street, Cambridge, MA 02138, USA
[5] Atacama Large Millimeter/Submillimeter Array, Joint ALMA Observatory, Alonso de Córdova 3107, Vitacura 763-0355, Santiago, Chile
[6] Departamento de Astronomía, Universidad de Chile, Camino El Observatorio 1515, Las Condes, Santiago, Chile
[7] Department of Physics and Astronomy, Rice University, 6100 Main Street, MS-108, Houston, TX 77005, USA
[8] NRAO, 520 Edgemont Road, Charlottesville, VA 22903, USA
Received 2019 October 15; revised 2020 January 9; accepted 2020 January 20; published 2020 February 10

Abstract

We present evidence for localized deviations from Keplerian rotation, i.e., velocity "kinks," in 8 of the 18 circumstellar disks observed by the DSHARP program: DoAr 25, Elias 2–27, GW Lup, HD 143006, HD 163296, IM Lup, Sz 129, and WaOph 6. Most of the kinks are detected over a small range in both radial extent and velocity, suggesting a planetary origin, but for some of them foreground contamination prevents us from measuring their spatial and velocity extent. Because of the DSHARP limited spectral resolution and signal to noise in the ^{12}CO $J = 2-1$ line, as well as cloud contamination, the kinks are usually detected in only one spectral channel, and will require confirmation. The strongest circumstantial evidence for protoplanets in the absence of higher spectral resolution data and additional tracers is that, upon deprojection, we find that *all* of the candidate planets lie within a gap and/or at the end of a spiral detected in dust continuum emission. This suggests that a significant fraction of the dust gaps and spirals observed by Atacama Large Millimeter/submillimeter Array in disks are caused by embedded protoplanets.

Unified Astronomy Thesaurus concepts: Protoplanetary disks (1300); Planet formation (1241); Submillimeter astronomy (1647)

1. Introduction

Since the first spectacular Atacama Large Millimeter/submillimeter Array (ALMA) images of HL Tau (ALMA Partnership et al. 2015), we have speculated about the origin of rings and gaps in disks. Proposed explanations include snow lines (e.g., Zhang et al. 2015), dust grain sintering (Okuzumi et al. 2016), non-ideal MHD effects and zonal flows (Flock et al. 2015; Riols & Lesur 2019), and self-induced dust-traps (Gonzalez et al. 2017). The most tantalizing explanation is that dust gaps are caused by embedded planets (Dipierro et al. 2015; Jin et al. 2016; Dong & Fung 2017; Zhang et al. 2018)

Direct imaging of putative planets in young circumstellar disks has proved difficult. After several years of surveys using the new generation of adaptive optics instruments, the only confirmed directly imaged protoplanets are located in the gap/cavity of the transition disk around PDS 70 (Keppler et al. 2018; Müller et al. 2018; Christiaens et al. 2019; Haffert et al. 2019).

A complementary approach is to search for kinematic signatures of planets. Embedded planets perturb the Keplerian gas flow in their vicinity, launching spiral waves at Lindblad resonances both inside and outside their orbits (Goldreich & Tremaine 1979). The disturbed velocity pattern is detectable with high spectral and high spatial resolution ALMA line observations (Perez et al. 2015). Accurate measurements of rotation curves revealed, for instance, radial pressure gradients and vertical flows, likely driven by gaps carved in the gas surface density by Jupiter-mass planets in the disk of HD 163296 (Teague et al. 2018a, 2019). In a given channel map, the emission is concentrated along the isovelocity curve,

i.e., the region of the disk where the projected velocity is constant. In the presence of a planet, the isovelocity is distorted and the emission displays a distinctive "kink." This technique led to the detection of embedded planets in the disks surrounding HD 163296 (Pinte et al. 2018b) and HD 97048 (Pinte et al. 2019), with masses 2–3 times that of Jupiter. Similarly, deviations from Keplerian rotation were detected in the disk of HD 100546 (Pérez et al. 2019).

In all three cases, the velocity kinks coincide with a gap, demonstrating that protoplanets are responsible for at least some of the gaps observed in disks. The recent spectacular series of ALMA high angular resolution campaigns (Huang et al. 2018a; Long et al. 2018; see also a collection of other data sets in van der Marel et al. 2019) have shown that rings and gaps are common, and they are now known in more than 30 disks. Are all of these gaps associated with protoplanets?

To answer this question, we have searched through existing ALMA archival data for kinks. Few data sets have the required signal-to-noise ratio, spectral and spatial resolution to reveal kinks, except the data from the DSHARP program (Andrews et al. 2018; Huang et al. 2018a). We find nine candidate kinks.

2. Observations and Imaging

We detected the velocity kinks by manually inspecting the publicly available, science-ready DSHARP ^{12}CO $J = 2-1$ data cubes.[9] We excluded HT Lup and AS 205 from our analysis as they are binary stars and display a perturbed velocity field.

---

[9] https://almascience.org/alma-data/lp/DSHARP

Continuum subtraction can significantly affect the measured brightness temperature and apparent morphology of line emission when the line is optically thick, and the line and continuum intensities are comparable (Boehler et al. 2017). To ensure that our kinks are not artificially created by continuum subtraction, we re-imaged all the CO data without continuum subtraction. For all disks, we used the released non-continuum-subtracted visibilities, and adapted the released scripts to re-image with the same parameters as the fiducial (continuum-subtracted) DSHARP images (see Table 5 in Andrews et al. 2018). The initial DSHARP data were imaged with a mix of manual masking and automasking. Here we used automasking in all cases, and for the disks that were imaged with manual masks in DSHARP, we also re-imaged the continuum-subtracted data to ensure that there was no significant differences with the original CO cubes. The kinks we present below are detected in both the continuum-subtracted and non-continuum-subtracted cubes in each case.

The channel width of the DSHARP data is 244 kHz. Due to Hanning smoothing, the velocity resolution is $640\,\mathrm{m\,s^{-1}}$. We re-imaged the cubes with the same channel spacing as the publicly released calibrated visibilities and fiducial DSHARP CO cubes: $350\,\mathrm{m\,s^{-1}}$, except for HD 163296 and HD 143006, which were imaged with a velocity spacing of $320\,\mathrm{m\,s^{-1}}$.

3. Results

We detect nine velocity kinks in 8 of the 18 selected DSHARP objects. Figures 1 and 2 show the continuum emission (left column) and three selected successive velocity channels (second, third, and fourth columns, respectively) in the ^{12}CO $J = 2-1$ emission for our nine candidate CO emission kinks. The third column shows the channel where the velocity kink is most prominently detected, with the kink itself indicated by the dotted white circle. The last column shows the CO emission in the channel at opposite velocity, demonstrating that the kink is not an axisymmetric feature. The kinks were identified by visual inspection of the CO cubes. There is currently no quantitative means of assessing confidence in a detection, when the signal-to-noise ratio is limited, and when background/foreground contamination exists as we are probing the disks in the ^{12}CO line.

We have grouped the detections according to the visual quality of the detection: *firm* detections in Figure 1 and *potential* detections in Figure 2. Independent observations will be required to confirm these candidate velocity kinks.

The DSHARP program was mostly aiming at high spatial resolution in continuum emission. The ^{12}CO $J = 2-1$ data only have a coarse spectral resolution of $\approx 640\,\mathrm{m\,s^{-1}}$, and were imaged at 0.″1 spatial resolution due to the low signal-to-noise ratio (Andrews et al. 2018). Most velocity kinks appear narrow in velocity, suggesting a local origin. The isovelocity curves overplotted in the central panel of Figures 1 and 2 show that in all cases, velocity perturbations are limited to 20% of the local Keplerian velocity. Across the kinks, the emission wiggles between the two isovelocity curves at $\pm 0.2\,v_{\mathrm{Kep}}$ without crossing them (except for HD 143006), indicating velocity deviations of order 10%–15%. The limited velocity resolution prevents unambiguous detections of the velocity kinks in every case. The kinks are seen to a lesser extent in the neighboring channels (second and fourth columns in Figures 1 and 2).

Assuming the velocity kink is caused by a planet, the cyan dot in each panel indicates the inferred location of the protoplanet when the velocity kink is deprojected to the disk midplane (using the method described in Pinte et al. 2018a to measure the CO emitting layer altitude). The location of the candidate protoplanets are indicated in Table 1. The detection in HD 143006 was already presented in Pérez et al. (2018), and the first one in HD 163296 in Pinte et al. (2018b) and Isella et al. (2018), but we also include them here for completeness.

In every case the candidate protoplanet would lie within a gap in the dust continuum emission. In two cases (IM Lup and WaOph 6) the protoplanet would also lie at the tip of a spiral arm detected in the dust continuum emission (Huang et al. 2018b). There is, however, no obvious correlation between the detection of a kink and spectral type, molecular cloud membership (as a proxy for age), or properties of the dust continuum gap.

Nondetections in the remaining 10 objects may be due to the limited signal-to-noise ratio and contamination of the ^{12}CO emission by surrounding clouds. In particular, emission in Sz 114, SR 4, Elias 2–20, Elias 2–24, and WSB 52 is contaminated, and the signal-to-noise ratio is low for MY Lup, HD 142666, and DoAr 33.

AS 209 and RU Lup are the only two sources that do not display any obvious CO emission kink despite modest cloud contamination and reasonable signal-to-noise ratio. The CO emission in RU Lup is contaminated by the outflow at large scales however, preventing any kink detection in the outer disk.

Perhaps surprisingly, we did not detect any obvious kink in AS 209, which is the DSHARP disk with the sharpest dust gaps (a small deviation might be present around $v = 3.7\,\mathrm{km\,s^{-1}}$), as well as with a gas gap detected outside of the continuum disk (Guzmán et al. 2018).

4. Discussion

4.1. Origin of the Velocity Kinks

Several observational effects and physical mechanisms may produce features in the channel maps that look like velocity kinks.

The most obvious one is the reconstruction process at low signal-to-noise ratio that often results in patchy emission that could be mistaken for kinks. We cannot exclude that such artifacts are present in the DSHARP data, but we indicate in Table 1 the measured signal-to-noise ratio at the location of the kink. We also imaged the cubes with deeper CLEANing, as well as different choices of *uv* taper, robust parameters, CLEANing scales, and velocity binning. The various changes to the imaging parameters do not significantly affect the kinks (see the Appendix). Deeper observations and in optically thinner tracers (less affected by cloud contamination) are needed to fully confirm these candidate detections.

Optical depth effects and in particular continuum subtraction may also affect the emission in a given channel, potentially mimicking a kink. Comparison of the continuum-subtracted and non-continuum-subtracted maps shows that this does not significantly affect our results. All kinks are recovered in both sets of maps, at the same location.

A locally reduced altitude of the CO emitting layer, for instance, due to an axisymmetric physical gap in the gas density structure, would also result in a displacement of the
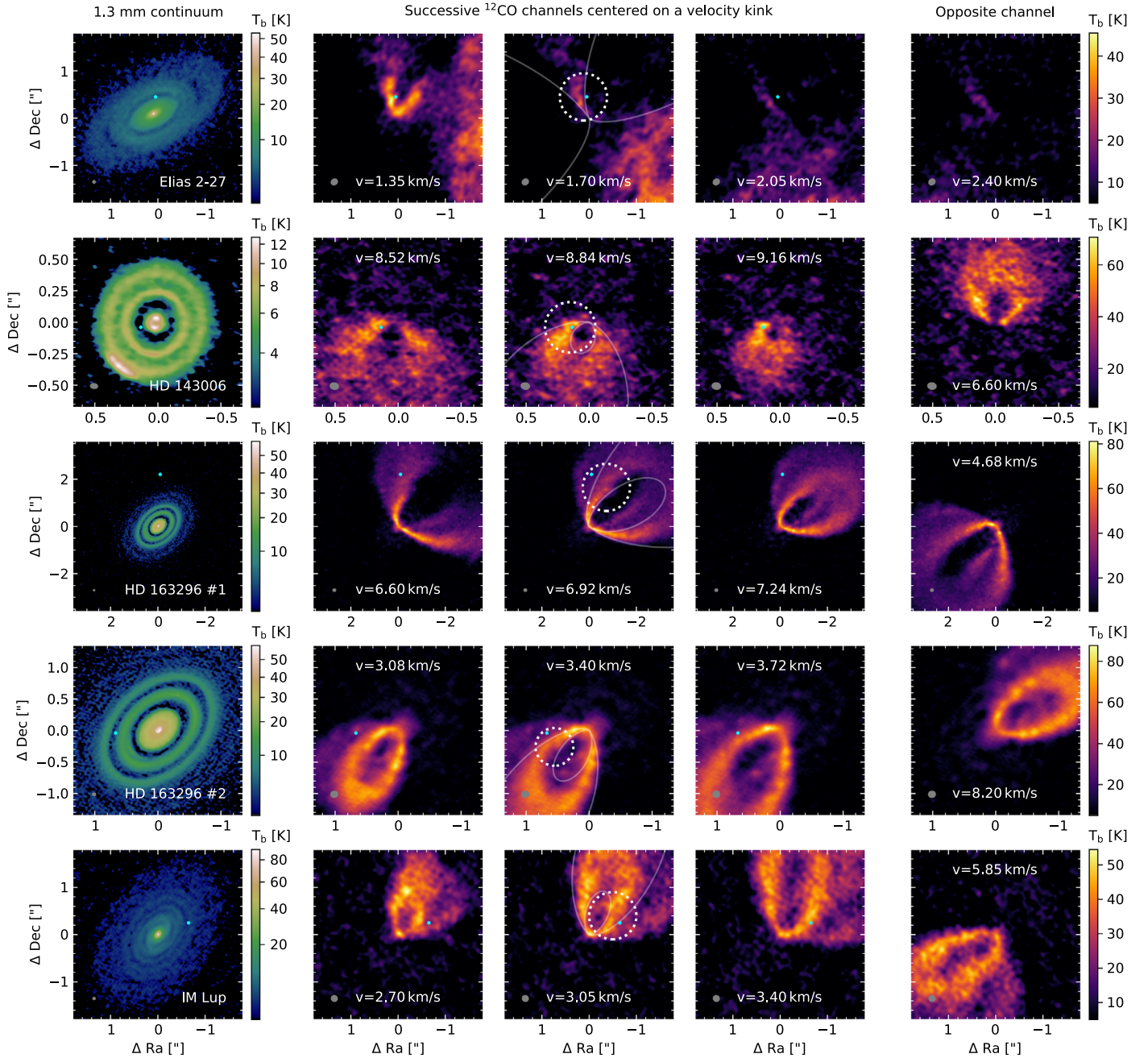
Figure 1. Candidate velocity kinks detected in the ^{12}CO $J = 2-1$ DSHARP data. Dashed circles indicate the velocity kinks, and the cyan dots the location of the planet assuming it is in the disk midplane. Solid lines in the third column indicate the expected location of the isovelocity curves at $\pm 0.2\, v_{\rm Kep} \sin i$, where $v_{\rm Kep}$ is the Keplerian velocity at the location of the planet. In all eight disks the candidate planet lies within a continuum dust gap. Note that channel spacing is half of the spectral resolution due to Hanning smoothing, and adjacent channels are not independent. Strong cloud contamination is present for Elias 2–27.

emission, but this distorted emission should be seen in all channels and should be associated with variations in brightness temperature. This is, for instance, seen for HD 163296, where gaps have been previously detected in the gas (Isella et al. 2016), in particular south of the star in the channels presented in Figure 1. The velocity kink we detect east of the central object displays a significantly different fork shape, but we cannot rule out that it is at least partly due to a CO line optical depth effect, rather than a velocity signature. Higher spectral resolution observation at a similar spatial resolution is necessary to conclusively distinguish between these two possibilities. Similarly, CO gaps have been detected by

Favre et al. (2018) in the disk of AS 209 and may hide the presence of small velocity kinks. Additionally, Teague et al. (2018b) measured azimuthally averaged rotation curves in AS 209 and detected deviations from Keplerian rotation at the 5% level. It remains unclear whether these deviations in the velocity profile reveal intrinsically azimuthally symmetric deviations or averaged localized deviations. As far as we can tell, there is no significant localized deviation in the velocity field of the disk as probed by ^{12}CO.

Non-Keplerian motion may be unrelated to planet wakes. The deviation from Keplerian velocity may occur in the radial, vertical, or azimuthal directions, or any combination thereof.
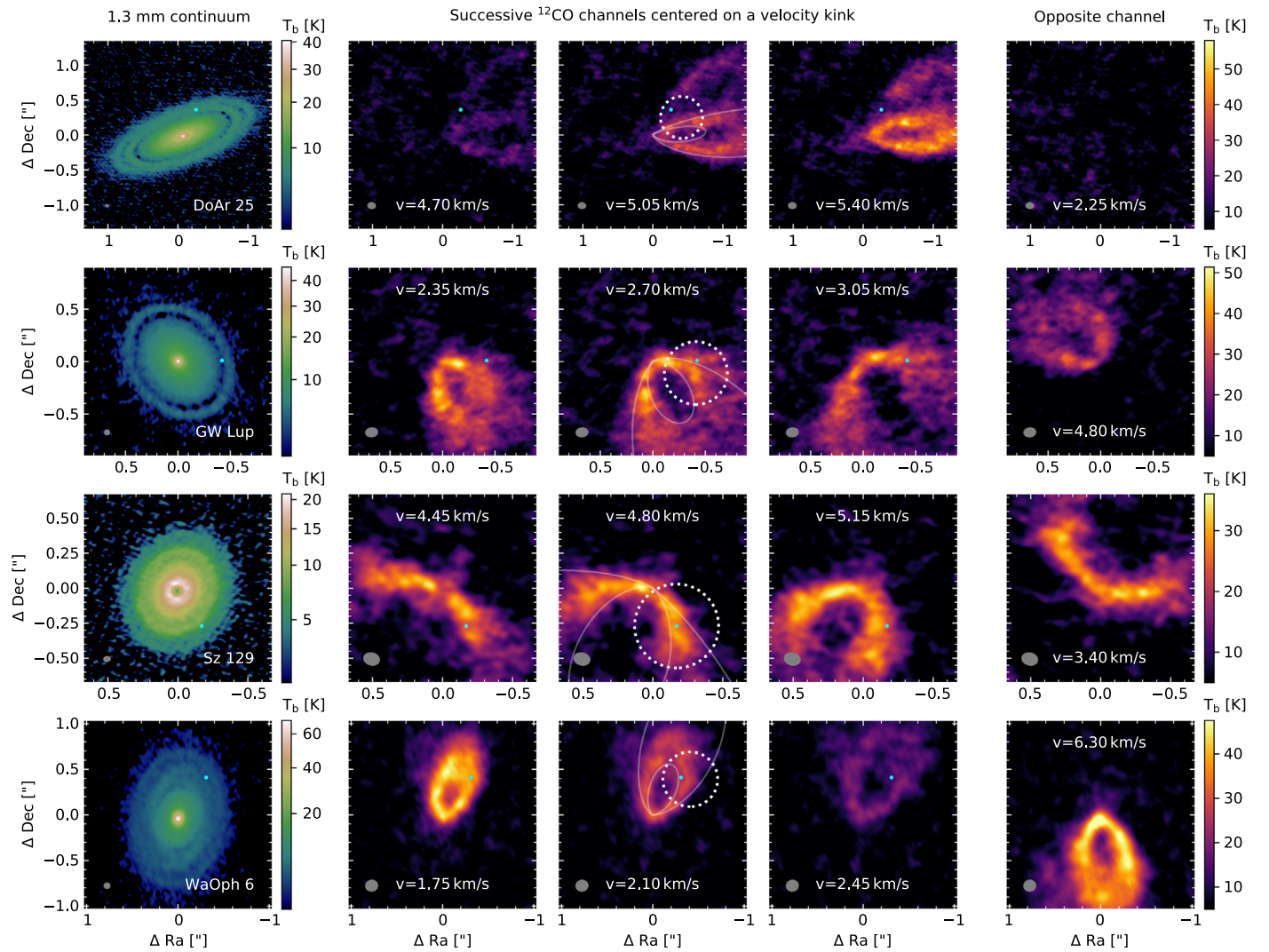
Figure 2. Additional potential velocity kinks. The detections are not as clear as in Figure 1 due to the lower-quality image reconstruction. Panels are the same as in Figure 1. Strong cloud contamination is present for DoAR 25 and WaOph 6.

Spiral arms caused by (internal or external) companions more massive than a planet or gravitational instabilities will also generate velocity perturbations. For instance deviations from Keplerian velocities in HD 142527 (Casassus et al. 2015; Price et al. 2018), and more recently HD 100546 (Pérez et al. 2019), likely reflect the presence of a massive companion ($\approx$0.3 $M_\odot$ for HD 142527 and $>10\,M_{\rm Jup}$ for HD 100546). The main difference is that large-scale spirals will produce velocity deviations over a significant fraction of the disk and a significant range of velocities (for instance $\approx$7 km s^{-1} for HD 100546; Pérez et al. 2019), whereas embedded planets would only produce a localized velocity kink.

Pressure gradients at the edge of the gap could also cause non-Keplerian motions, however such perturbations occur over a wide range in azimuth, which is not seen for any of our candidate detections above.

Foreground extinction in ^{12}CO sometimes makes it difficult to assess if velocity kinks seen in the DSHARP data are localized (in both space and velocity). We indicate in Table 2 when this is the case. None of our detections are extended over a significant fraction of the disk, but some of them are strongly extincted or

confused with cloud emission, preventing us from ruling out a large-scale velocity feature. The most obvious cases are DoAr 25, Elias 2–27, and WaOph 6 where the channels adjacent to the main channel where the kink is detected are heavily extincted. If the cloud contamination is not uniform across the disk, this may artificially create an apparent kink by distorting the disk emission. We also detected hints of velocity deviations on the south side of Elias 2–27, but the ^{12}CO emission is diffuse making it impossible to reach a definitive conclusion. More optically thin molecular lines should provide a more definitive answer.

Because the velocity deviations created by an embedded planet are small (around 10% of the Keplerian velocity for a Jupiter-mass planet at a few tens of au), a planet kink can often only be detected in a single channel at the DSHARP spectral resolution ($\approx$640 m s^{-1}), making it difficult to assess whether the detection is robust or whether it is affected by imaging artifacts. For HD 163296 and HD 97048 (Pinte et al. 2018b, 2019), the high velocity resolution ($\approx$100–200 m s^{-1}) enabled detection of the kinks in several subsequent channels, providing for robust detections.

Table 1
Summary of Candidate Protoplanets

Object	Planet Sep. ($''$)	Planet PA (deg)	S/N[a]	Velocity Width Δv (m s^{-1})	$\Delta v/v_{\mathrm{Kep}}$	Gap Radius (au)	Gap Width Δ/r	M_{star} ($M_\odot$)	Distance (pc)	Planet Location
Elias 2–27	0.32	-6	12	?	?	69	0.18	0.49	116^{+19}_{-10}	Semiminor axis
HD 143006	0.14	-107	10	$\approx$700	$\approx$0.20	22	0.62	1.78	165 ± 5	Redshifted near side
HD 163296	2.20	3	27	$<$700	$<$0.26	260	$\cdots$	2.04	101 ± 2	Redshifted near side
HD 163296	0.67	-93	36	$\approx$700	$\approx$0.15	86	0.17	2.04	101 ± 2	Blueshifted near side
IM Lup	0.70	69	14	$<$700	$<$0.24	117	0.13	1.12	158 ± 3	Blueshifted near side
DoAr 25	0.44	36	7	?	?	98	0.15	0.95	138 ± 3	Redshifted near side
GW Lup	0.42	89	12	$<$700	$<$0.3	74	0.15	0.46	155 ± 3	Blueshifted near side
Sz 129	0.29	148	11	$<$700	$<$0.2	64	$\cdots$	0.83	161 ± 3	Redshifted far side
WaOph 6	0.51	37	13	?	?	79	$\cdots$	0.68	123 ± 2	Blueshifted far side

Notes. Distances and stellar masses are as listed in Andrews et al. (2018). Gap widths are from Huang et al. (2018a). The signal to noise is the ratio of the signal at the location of the kink divided by the rms of the image far from the disk.

[a] Signal to noise of the CO emission at the location of the velocity kink.

Table 2
Summary of Candidate Kinks Assessed Against Our Four Criteria to Assess a Planetary Origin

Candidate Kink	Indep. of Cont. Sub.[a]	S/N > 10	Localized[b]	Resolved in v[c]
Elias 2–27	✓	✓	?	✓
HD 143006	✓	✗	✓	✓
HD 163296	✓	✓	✓	✓
HD 163296 #2	✓	✓	✓	✗
IM Lup	✓	✓	✓	✗
DoAr 25	✓	✗	?	?
GW Lup	✓	✓	✓	✗
Sz 129	✓	✓	✓	✗
WaOph 6	✓	✓	?	?

Notes.
[a] Detected in continuum-subtracted and non-subtracted data.
[b] Localized in space ($\lesssim 3$ beams) and velocity ($\lesssim 20\%$ Keplerian velocity).
[c] Detected in at least three independent channels.

4.2. A Planetary Origin?

Based on the arguments presented above, for a velocity kink to be caused by a planet the perturbation should be, at minimum, (i) detected in continuum-subtracted and non-continuum-sub-tracted data, (ii) detected at high signal-to-noise ratio, (iii) localized in velocity (e.g., to within 20% of the local Keplerian velocity) and space (e.g., to within three beams), and (iv) resolved in velocity (i.e., detected in at least three independent channels). In Table 2 we assess our nine candidate kinks against these four criteria. Only the main kink seen in HD 163296 at 2″2 satisfies all four criteria with the currently available data sets. The remaining uncertainty is due to the poor quality of the data rather than specifically ruling out a planetary origin.

The most compelling argument toward a planetary origin is that, when deprojected, all nine kinks point to a perturber located in a continuum dust gap and, in two cases, at the tip of a spiral arm. There is an increasing consensus (mainly from theoretical modeling efforts) that dust gaps seen with ALMA are caused by embedded bodies (e.g., Dong et al. 2015; Bae et al. 2017; Zhang et al. 2018; Lodato et al. 2019), so detection of perturbing bodies in ALMA kinematics is not unexpected. We emphasize that this deprojection was performed blind in the continuum-subtracted channel maps, i.e., without reference to the dust gap locations (Pinte et al. 2018a).

The velocity kinks we detected are not uniformly distributed in azimuth in the disks. In particular, we did not find any along the disk semimajor axis and only one along the semiminor axis (Table 1). Foreground contamination, when present, usually encompasses the systemic velocity, and often hides emission along the semiminor axis. Additionally, the distortions in the channel maps depend on the inclination, distance, and azimuth of the planets. Figure 3 shows the detectability of a planet-induced velocity deviation as a function of the planet azimuth. We used the disk model presented in Pinte et al. (2018b) for HD 163296, with a $3\,M_{\rm Jup}$ planet at 260 au. They appear stronger in the redshifted half of the near side of the disk (as well as the blueshifted half of the far side), but appear with smaller amplitude on the other half of the disk. Velocity perturbations are most difficult to detect along the semimajor axis, where they appear as a small tail originating from the planet tracing the spiral arm. In this region of the disk, i.e.,

near the tip of the isovelocity loop, emission is diffuse making it difficult to detect such a signal in actual data.

Casassus & Pérez (2019) suggested that the location of the planet could be pinpointed by searching for "Doppler flips" in the rotation map of the disk, after subtraction of the Keplerian rotation. For each position of the planet in Figure 3, we computed the moment 1 map and subtracted an azimuthally averaged model (implemented by rotating each particle in the smoothed particle hydrodynamics simulation by a random angle in the disk plane prior to performing the radiative transfer). The corresponding differential rotation maps are presented in the last two rows of Figure 3. In each panel, there is a sign reversal as suggested by Casassus & Pérez (2019), but the amplitude is small, with maximal deviations of about $150\,{\rm m\,s^{-1}}$. The Doppler flip is also dependent on the planet azimuth, with blueshifted and redshifted sides varying in amplitude and size. Some additional velocity sign reversals are also sometimes seen in other regions of the disk, potentially complicating the extraction of the planet position. The rotation maps presented in Figure 3 were generated with a perfect knowledge of the velocity field and taking into account the radiative transfer effects at the emitting surface. For actual data, the velocity field and altitude of the emitting layers have to be estimated. Uncertainties in the Keplerian velocity model that is subtracted may limit the detectability of Doppler flips to high signal-to-noise cases. In particular, the predicted Doppler flip for the orientation of HD 163296 (labeled panel in Figure 3) shows an amplitude twice smaller ($\approx 150\,{\rm m\,s^{-1}}$) than the residuals in the differential rotation map presented in Casassus & Pérez (2019) ($\approx 300\,{\rm m\,s^{-1}}$). This explains why they did not detect the counterparts of the kink as a Doppler flip in the first moment map. The absence of visible Doppler flip corresponding to the kink in HD 97048 is also not surprising given the residuals in the differential rotation maps presented by Casassus & Pérez (2019).

Because of the tentative nature of the detections and the need for higher-resolution observations, we are not yet confident enough to estimate planet masses from the candidate kinks seen in the DSHARP data. Detailed hydrodynamical and radiative transfer modeling of the kink candidates is currently the only way to determine planet masses from velocity deviations in a quantitative manner but would result in poorly constrained estimates given the low signal-to-noise ratio and poor velocity resolution of the data. We estimated the velocity deviations from the number of channels in which the kinks are detected. The limited spectral resolution prevents us from measuring velocity deviations smaller than $640\,{\rm m\,s^{-1}}$. By comparing with the expected location of the isovelocity curves if the disks were in Keplerian rotation, we estimate the observed perturbations to be of the order of 10%–15% of the local Keplerian velocity (Table 1). From our previous modeling of velocity kinks, we expect masses of the order of 1–3 $M_{\rm Jup}$. In HD 143006, the velocity deviation appears significantly larger, pointing toward a more massive planet.

With the exception of HD 143006, such masses are larger by a factor of 4–10 than the masses derived from the continuum gaps by Zhang et al. (2018) or Lodato et al. (2019). We found a similar discrepancy for HD 97048 (Pinte et al. 2019), where to get a coherent match to both the continuum and line data, our models required the dust grains dominating the emission to have a Stokes number of a few 10^{-2}, suggesting very porous and/or fluffy aggregates.
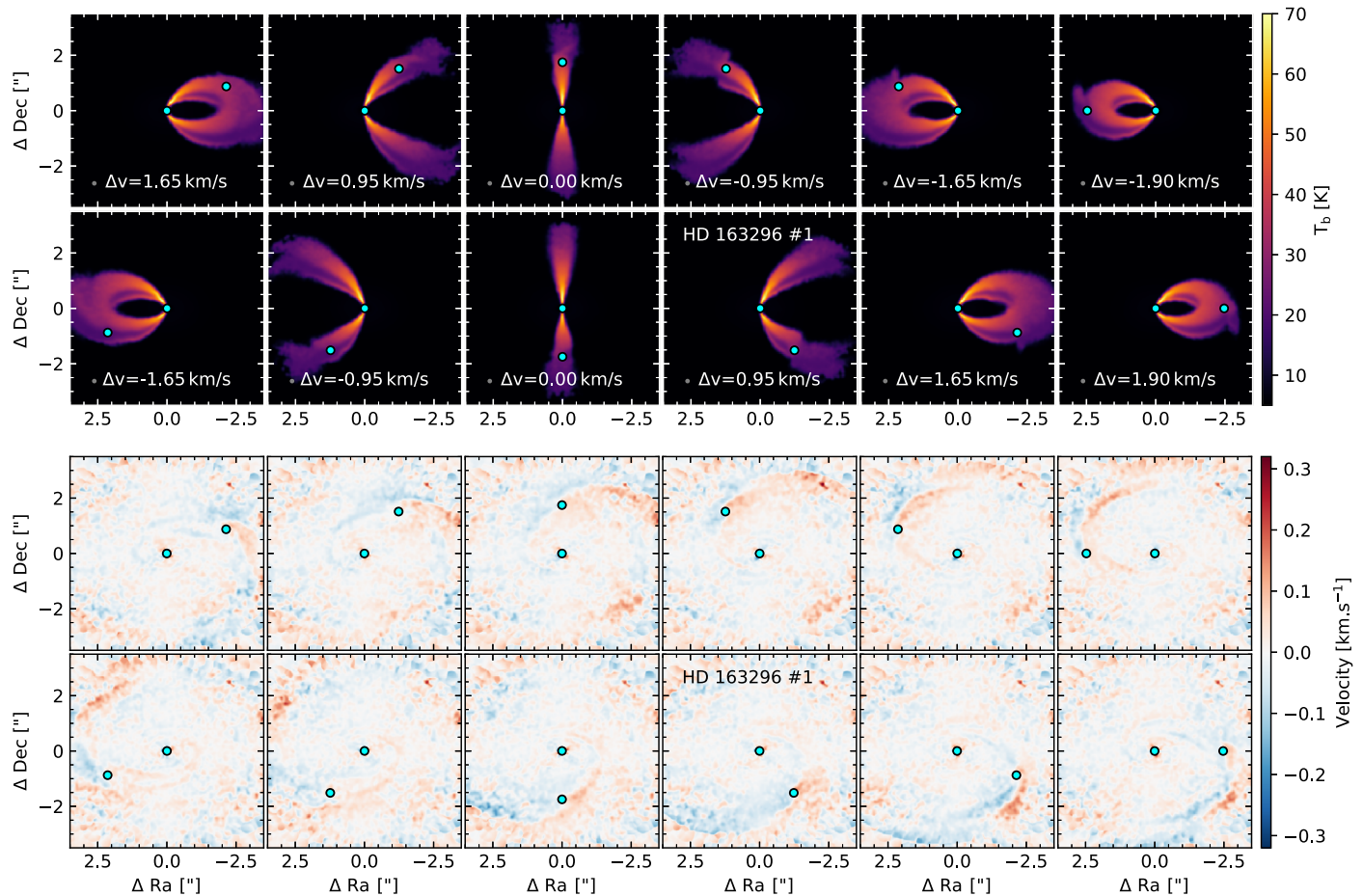
Figure 3. Detectability of a 3 M_{Jup} planet-induced deviation from Keplerian rotation as a function of planet azimuth. Disk semimajor axis is horizontal with near side toward the bottom of each panel. Planet is rotated by 30° between each panel. Models have been convolved by a Gaussian beam with an FWHM of 0.″1. Sink particles are marked by a cyan dot. The labeled panel indicates the configuration of the main kink of HD 163296 (with a different PA). Top two rows: ^{12}CO synthetic channel maps with a width of 50 m s^{-1}. In each panel, the velocity channel is selected to be the closest to the radial velocity of the planet. Bottom two rows: differential rotation maps for the same planet positions. In each panel, we compute the first moment of the model from which we subtract an azimuthally averaged model. The amplitude of the colormap corresponds to the DSHARP data velocity resolution (640 m s^{-1}).

The high detection rate of velocity kinks at several tens of astronomical units in the DSHARP data set may appear in contradiction with the occurrence rate of known giant extrasolar planets at large distance from their host stars: in the range of a few up to 5% for massive planets ($M > 2\,M_{Jup}$) beyond 10–20 au (Vigan et al. 2017; Nielsen et al. 2019). This occurrence rate suffers from large uncertainties, however, depending on the assumption of a hot- or cold-start model for the planet. For instance, using cold-start models, Stone et al. (2018) find that up to 90% of FGK systems can host a 7–10 M_{Jup} planet from 5 to 50 au. Part of this discrepancy could also reflect the selection biases of the DSHARP program, which was aimed at millimeter bright protoplanetary disks. This could in turn be biased toward objects that have formed massive planets at large radii. Additionally, the DSHARP planets will likely migrate inward by the time the disk dissipates. Assuming one planet per gap and modeling the planet orbital evolution and accretion, Lodato et al. (2019) found that the final distribution of the planets from the DSHARP sample (as well as the Taurus survey; Long et al. 2018) is consistent with the known properties of the exoplanet population, and would represent a good match to the distribution of cold Jupiters.

5. Conclusions

1. We found nine localized (channel-specific) velocity perturbations indicative of non-Keplerian motion in DSHARP observations of 8 protoplanetary disks, out of the 18 selected sources.

2. When deprojected, we find that the velocity kinks are systematically associated with gaps seen in continuum emission, suggesting they share a common origin. The presence of embedded planets would naturally explain both the continuum rings and gas velocity deviations from Keplerian rotation.

3. If planets are indeed responsible for these tentative velocity kinks, they should have masses of the order of a Jupiter mass. This is 4 to 10 times higher than the estimates from the width and depth of the continuum gaps.

4. Limited spectral resolution and signal-to-noise ratio, as well as cloud contamination, prevent us from reaching definitive conclusions in several cases. In particular, nondetections in other disks or in other gaps in disks where we detected a kink do not necessarily imply the absence of Jupiter-mass planets.

5. Synthetic models indicate that the shape and amplitude of the planet velocity kink in the channel maps and rotation maps depend on the system geometry, inclination, azimuth, and distance of the planet. In particular, for a given planet, signatures appear fainter on the blueshifted half of the near side and redshifted half of the far side of the disk, as well as along the disk semimajor axis. This suggests additional planet signatures could be found with higher signal-to-noise data.

High signal-to-noise follow-up mapping at similar spatial resolution to the DSHARP data ($\approx 0\rlap{.}''1$) and at high spectral resolution ($\approx 100\,\mathrm{m\,s^{-1}}$) can be reached with ALMA for less abundant molecules, i.e., with less foreground/background contamination, than ^{12}CO with integration times ranging from 2–4 hr (^{13}CO) to 10–20 hr (e.g., $C^{18}O$, HCO^+). Such observations would confirm the tentative detections presented above and enable us to characterize the embedded planets.

Appendix
Imaging Tests

Given the low signal-to-noise and limited *uv* coverage of the DSHARP CO observations (which were designed with the continuum as the primary goal), the synthesis imaging limitations can potentially create artifacts that mimic a velocity kink. Figures 4–12 illustrate the imaging tests we have performed. In all cases, the velocity kink remains detected.

The discontinuities in the gridded *uv* weight density when imaging the combined data from several ALMA configurations result in non-Gaussian beams with significant "shelves" (e.g., Jorsater & van Moorsel 1995). This may affect the flux of the image as the clean model is convolved with the clean beam (units Jy/clean beam), while the dirty image and residuals are both in units of Jy/dirty beam. When the beam is Gaussian, these beam areas are equivalent, but when the beam has shelves, the integrated areas quickly diverge. In the case of the DSHARP data, the beam areas differ by about 20%. Panel (c) of Figures 4–12 shows an image where we convolved the clean model with a beam that matches the area of the dirty beam.

Narrow velocity deviations can be washed out if they are separated over two velocity bins. We re-imaged the cubes with an offset of half a frequency bin (i.e., 1/4 of the spectral resolution) compared to the fiducial DSHARP cubes (e.g., panels (h) and (i) of Figures 4 to 12). In all cases, we detect the velocity kinks in the "shifted" cubes with a similar significance, except for IM Lup where the kink appears sharper than in the fiducial DSHARP cube (Figure 8).
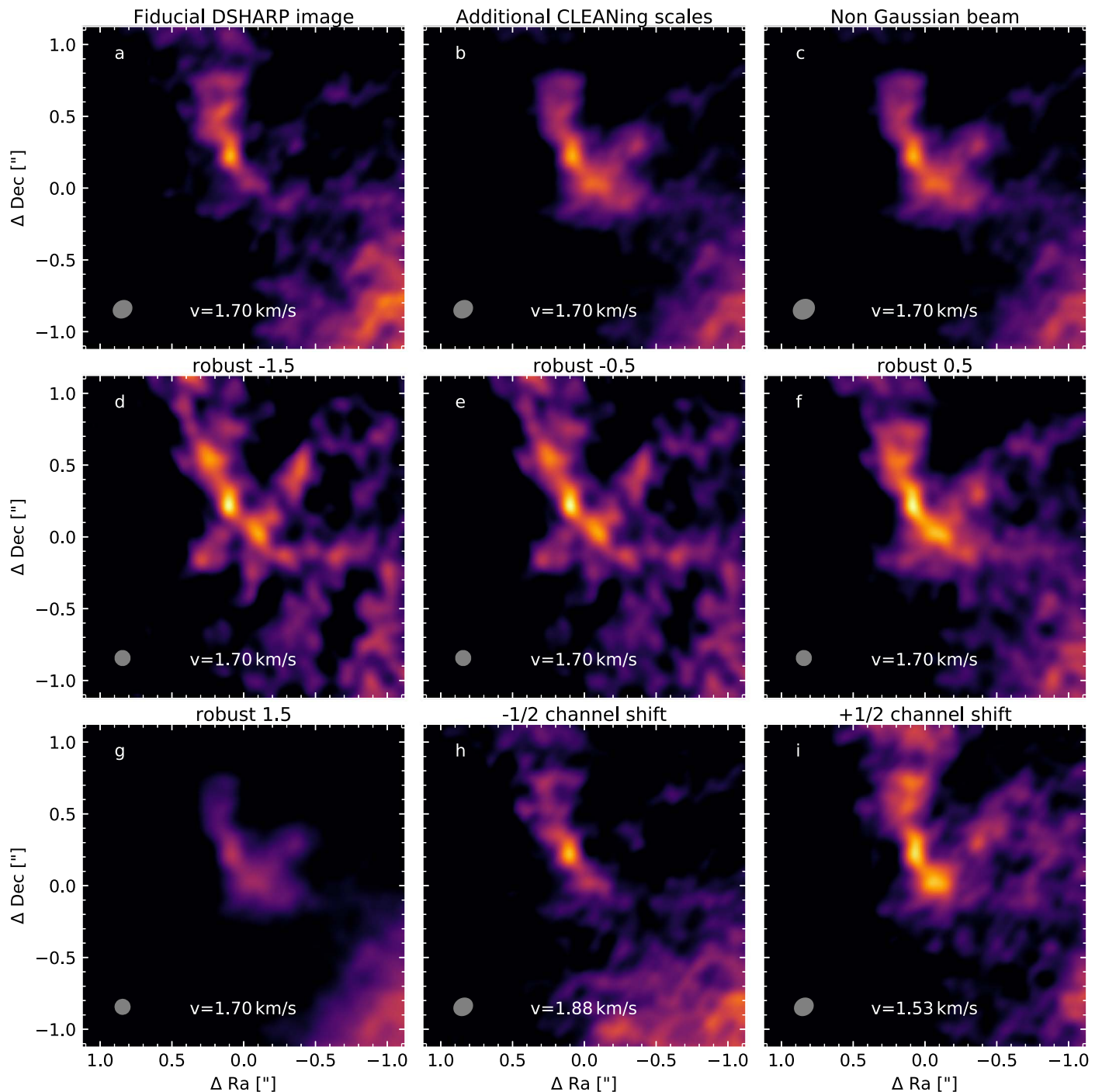
Figure 4. Imaging of Elias 2–27 with different parameters. (a) Fiducial DSHARP image (but without continuum subtraction). (b) Multiscale CLEANing was performed with scales of 0, 5, 10, 20, 40, 80, 160, 320, instead of 0, 10, 25, 75, 150. (c) Image generated by convolving the CLEAN model with a Gaussian beam of the same area as the dirty beam to take into account the wings of the beam generated by the combination of different ALMA configurations. (d)–(g) CLEANing was performing with increasing values of the robust parameter. Images were then convolved by a Gaussian beam to reach the same $0\rlap{.}''1$ spatial resolution. (h) and (i) Imaging was performed with the same setup as the fiducial image but at velocities shifted by $1/2$ of a channel ($\approx 1/4$ of the velocity resolution).
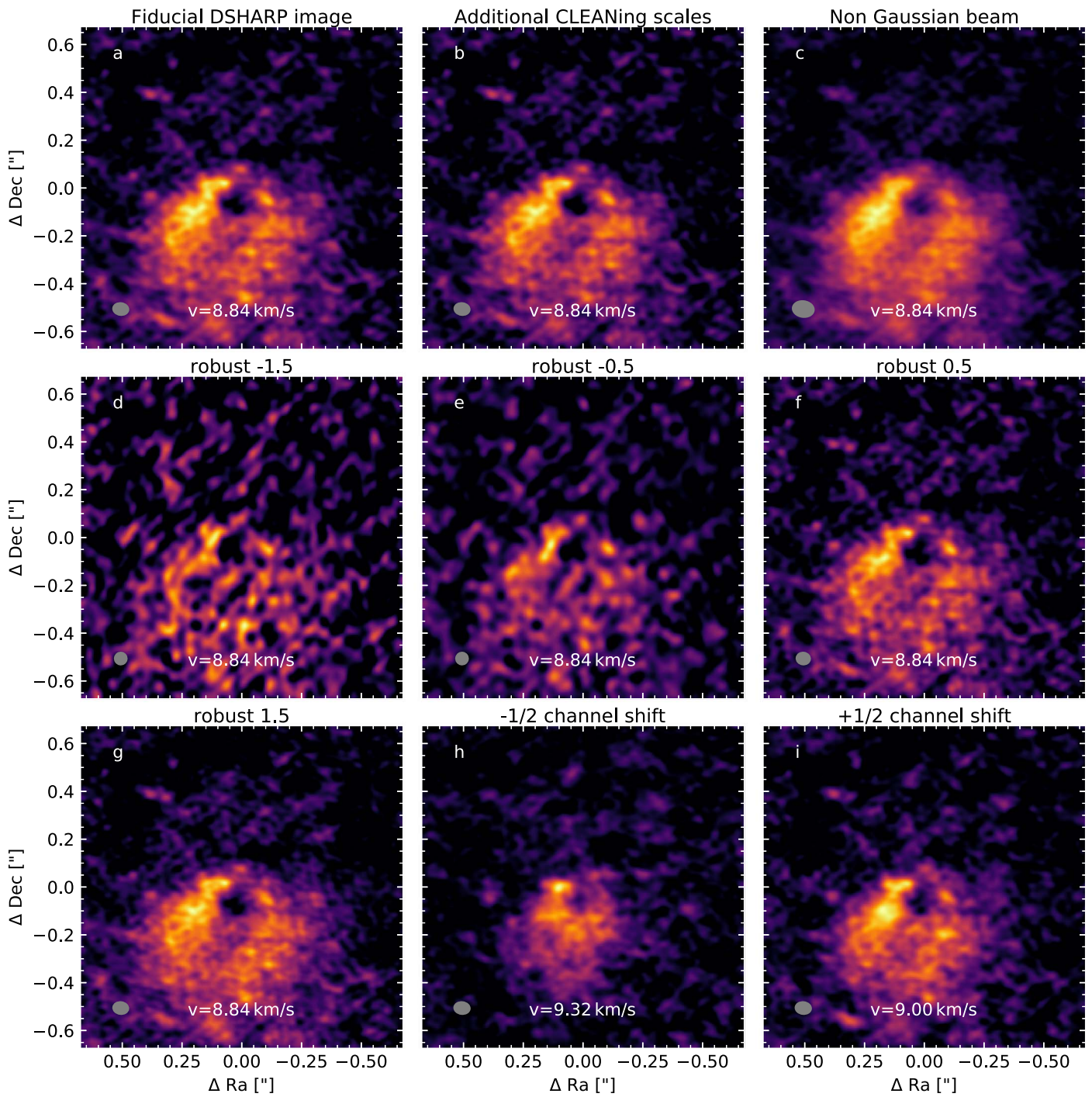
Figure 5. Same as Figure 4, but for HD 143006.
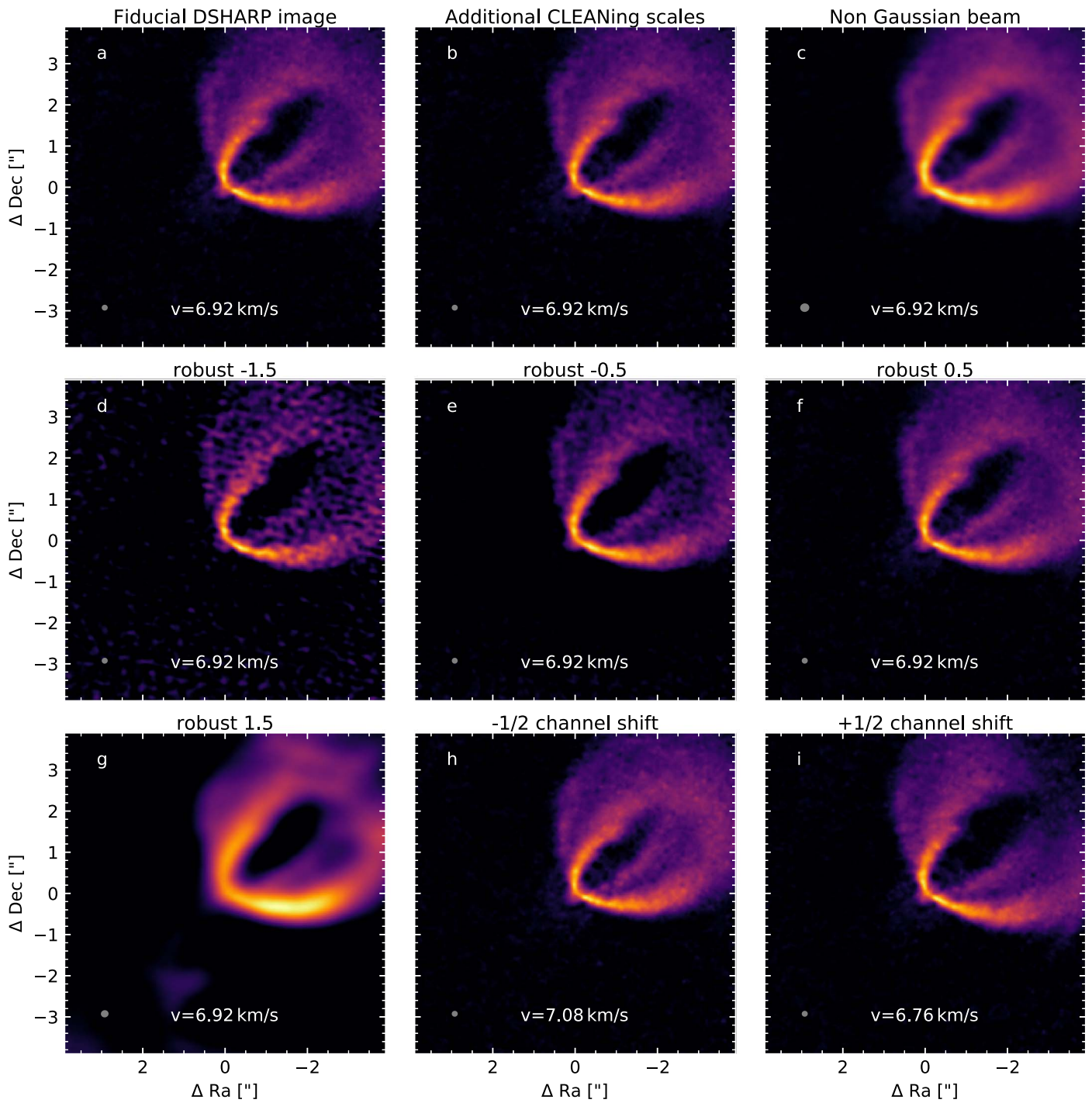
Figure 6. Same as Figure 4, but for HD 163296 #1.
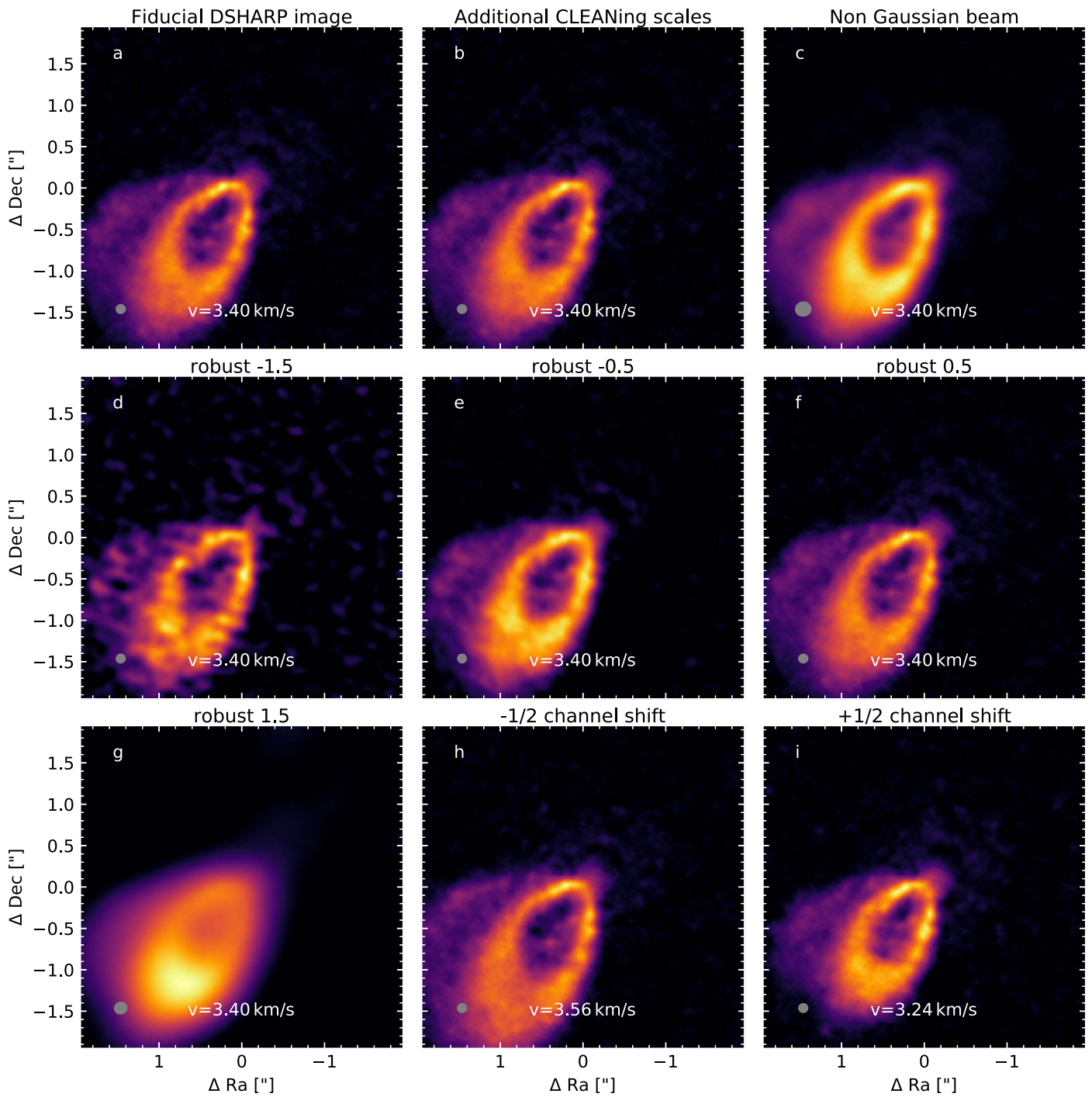
Figure 7. Same as Figure 4, but for HD 163296 #2.
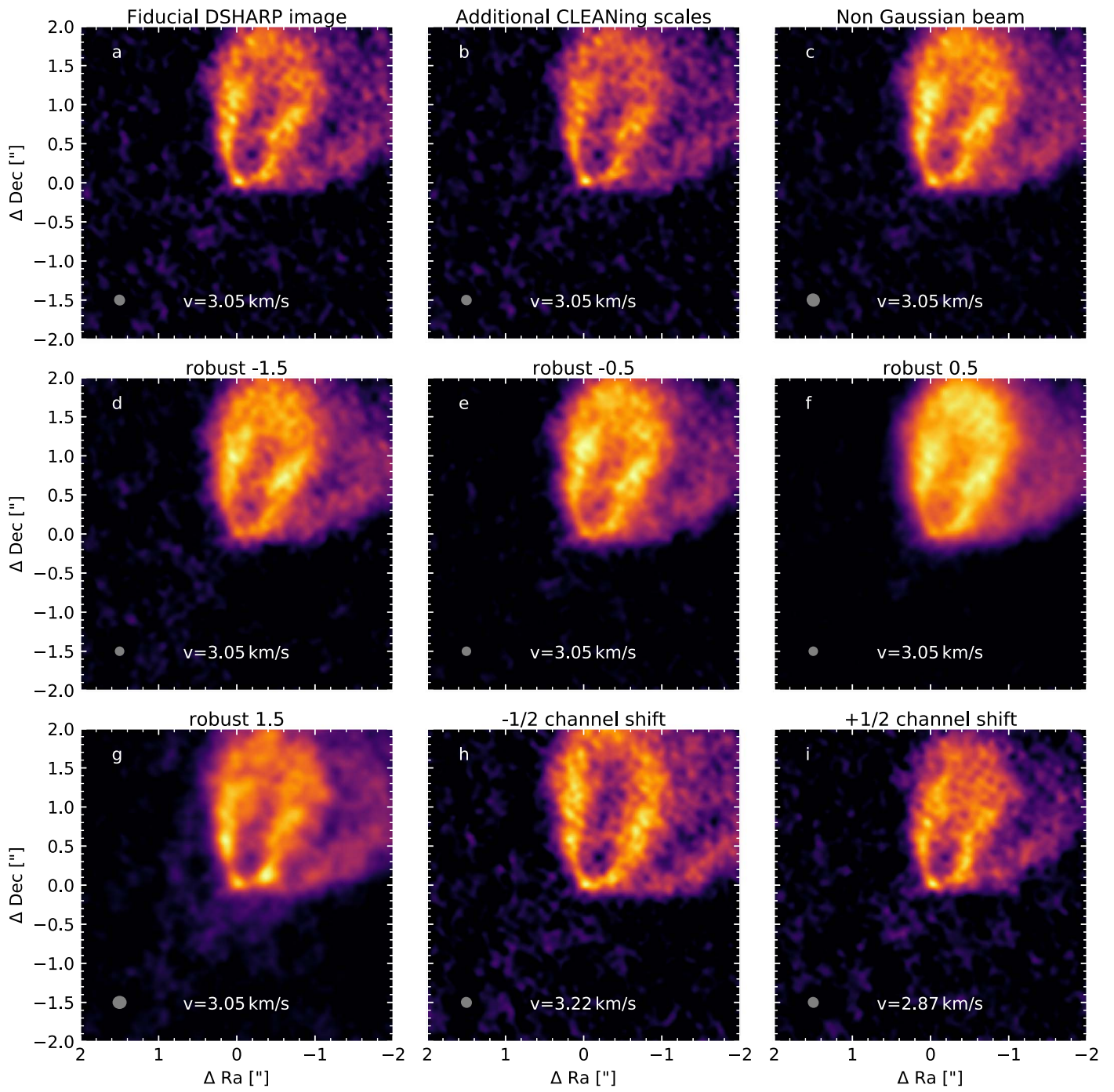
Figure 8. Same as Figure 4, but for IM Lup.
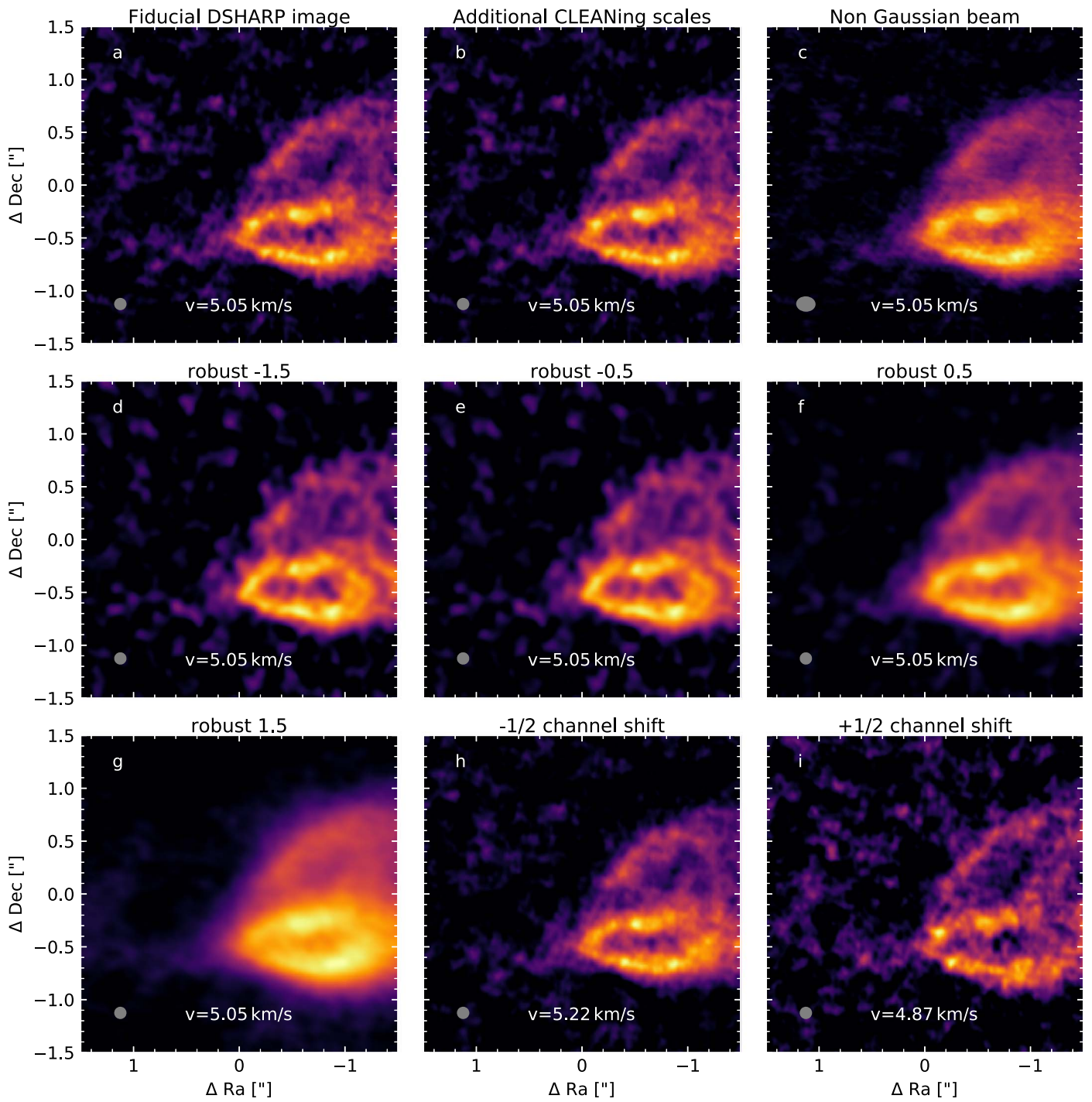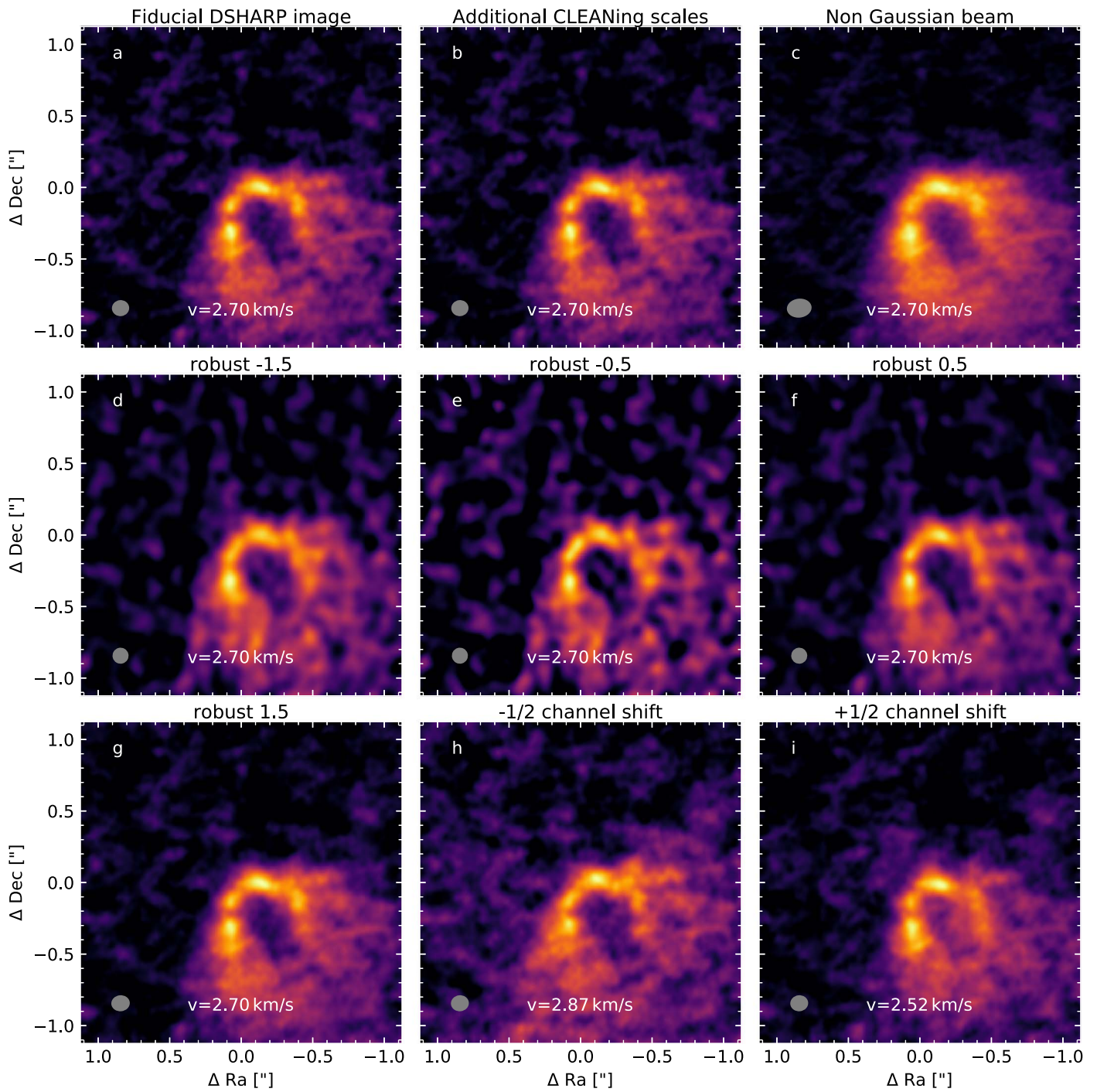
Figure 9. Same as Figure 4, but for DoAr 25.
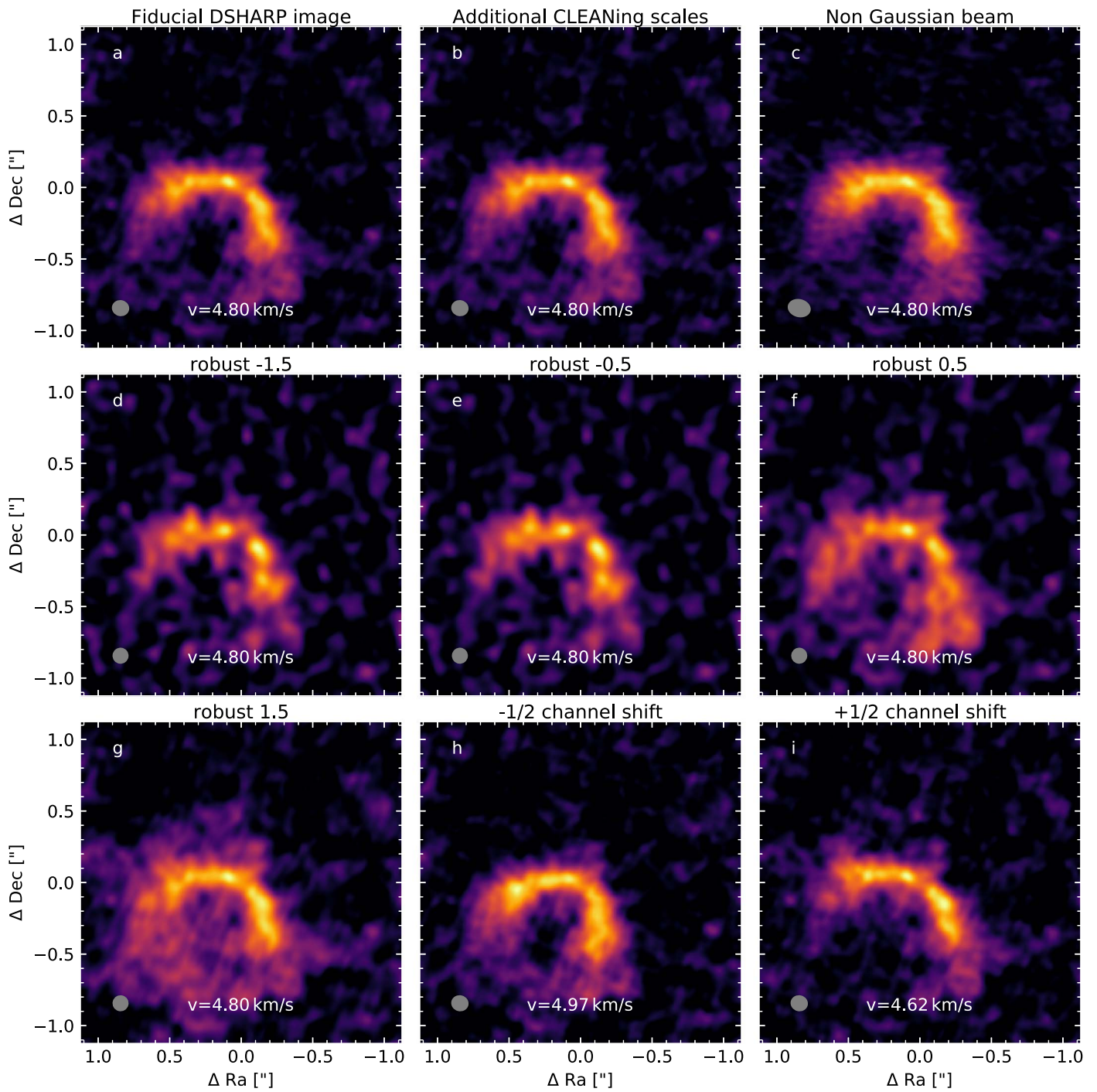
Figure 10. Same as Figure 4, but for GW lup.

Figure 11. Same as Figure 4, but for Sz 129.
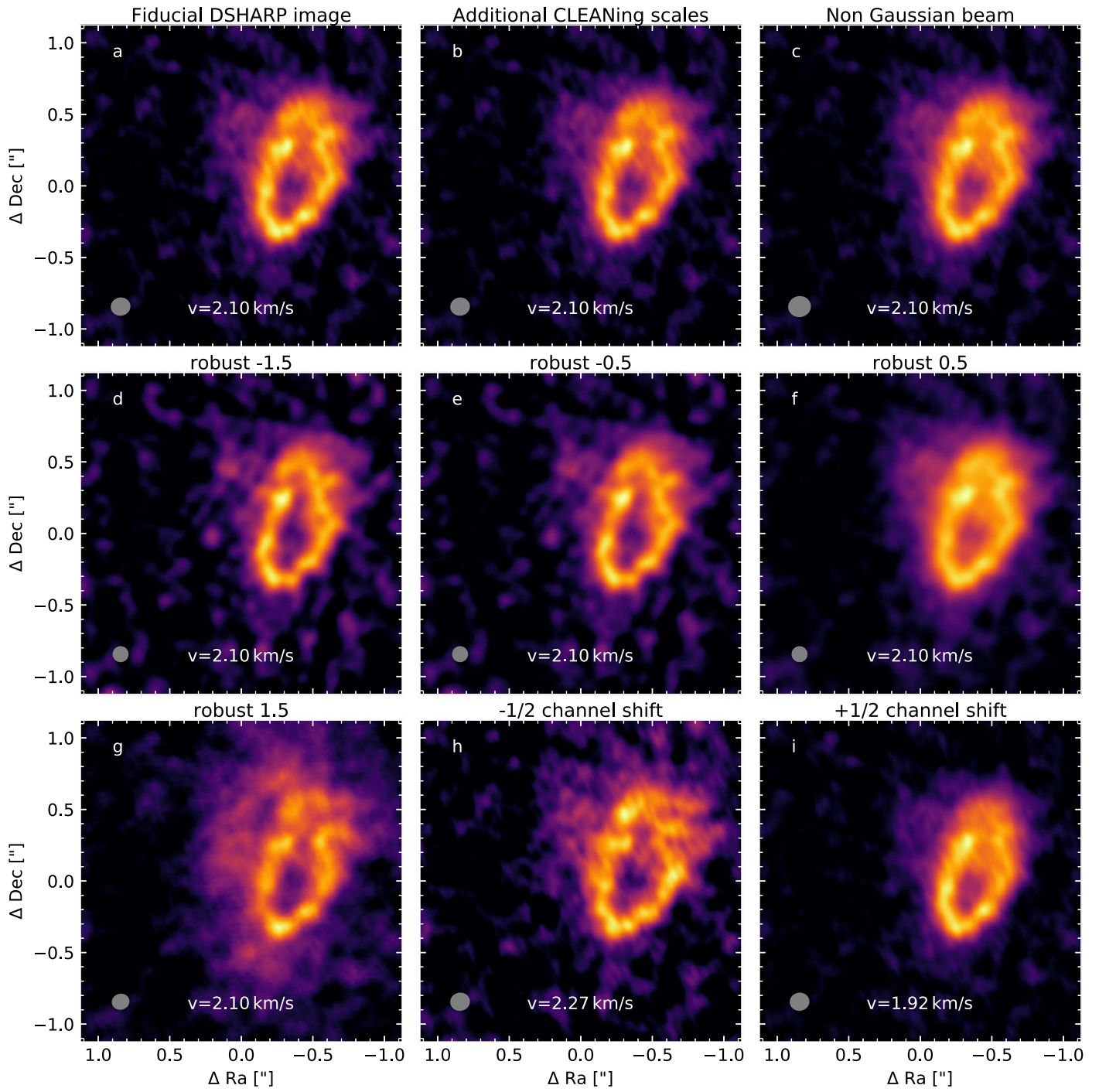
Figure 12. Same as Figure 4, but for WaOph 6.

ORCID iDs

C. Pinte ⓘ https://orcid.org/0000-0001-5907-5179
D. J. Price ⓘ https://orcid.org/0000-0002-4716-4235
F. Ménard ⓘ https://orcid.org/0000-0002-1637-7393
G. Duchêne ⓘ https://orcid.org/0000-0002-5092-6464
V. Christiaens ⓘ https://orcid.org/0000-0002-0101-8814
S. M. Andrews ⓘ https://orcid.org/0000-0003-2253-2270
J. Huang ⓘ https://orcid.org/0000-0001-6947-6072
T. Hill ⓘ https://orcid.org/0000-0003-3253-1255
G. van der Plas ⓘ https://orcid.org/0000-0001-5688-187X
L. M. Perez ⓘ https://orcid.org/0000-0002-1199-9564
A. Isella ⓘ https://orcid.org/0000-0001-8061-2207
Y. Boehler ⓘ https://orcid.org/0000-0002-8692-8744
D. Mentiplay ⓘ https://orcid.org/0000-0002-5526-8798
R. A. Loomis ⓘ https://orcid.org/0000-0002-8932-1219

References

ALMA Partnership, Brogan, C. L., Pérez, L. M., et al. 2015, ApJL, 808, L3
Andrews, S. M., Huang, J., Pérez, L. M., et al. 2018, ApJL, 869, L41
Bae, J., Zhu, Z., & Hartmann, L. 2017, ApJ, 850, 201
Boehler, Y., Weaver, E., Isella, A., et al. 2017, ApJ, 840, 60
Casassus, S., & Pérez, S. 2019, ApJL, 883, L41
Casassus, S., Marino, S., Pérez, S., et al. 2015, ApJ, 811, 92
Christiaens, V., Casassus, S., Absil, O., et al. 2019, MNRAS, 486, 5819
Dipierro, G., Price, D., Laibe, G., et al. 2015, MNRAS, 453, L73
Dong, R., & Fung, J. 2017, ApJ, 835, 146
Dong, R., Zhu, Z., & Whitney, B. 2015, ApJ, 809, 93
Favre, C., Fedele, D., Maud, L., et al. 2018, ApJ, 871, 107
Flock, M., Ruge, J. P., Dzyurkevich, N., et al. 2015, A&A, 574, A68
Goldreich, P., & Tremaine, S. 1979, ApJ, 233, 857
Gonzalez, J.-F., Laibe, G., & Maddison, S. T. 2017, MNRAS, 467, 1984
Guzmán, V. V., Huang, J., Andrews, S. M., et al. 2018, ApJL, 869, L48
Haffert, S. Y., Bohn, A. J., de Boer, J., et al. 2019, NatAs, 3, 749
Huang, J., Andrews, S. M., Dullemond, C. P., et al. 2018a, ApJL, 869, L42
Huang, J., Andrews, S. M., Pérez, L. M., et al. 2018b, ApJL, 869, L43
Isella, A., Guidi, G., Testi, L., et al. 2016, PhRvL, 117, 251101
Isella, A., Huang, J., Andrews, S. M., et al. 2018, ApJL, 869, L49
Jin, S., Li, S., Isella, A., Li, H., & Ji, J. 2016, ApJ, 818, 76
Jorsater, S., & van Moorsel, G. A. 1995, AJ, 110, 2037
Keppler, M., Benisty, M., Müller, A., et al. 2018, A&A, 617, A44
Lodato, G., Dipierro, G., Ragusa, E., et al. 2019, MNRAS, 486, 453
Long, F., Pinilla, P., Herczeg, G. J., et al. 2018, ApJ, 869, 17
McMullin, J. P., Waters, B., Schiebel, D., Young, W., & Golap, K. 2007, in ASP Conf. Ser. 376, Astronomical Data Analysis Software and Systems XVI, ed. R. A. Shaw, F. Hill, & D. J. Bell (San Francisco, CA: ASP), 127
Müller, A., Keppler, M., Henning, T., et al. 2018, A&A, 617, L2
Nielsen, E. L., De Rosa, R. J., Macintosh, B., et al. 2019, AJ, 158, 13
Okuzumi, S., Momose, M., Sirono, S.-I., Kobayashi, H., & Tanaka, H. 2016, ApJ, 821, 82
Pérez, L. M., Benisty, M., Andrews, S. M., et al. 2018, ApJL, 869, L50
Pérez, S., Casassus, S., Hales, A., et al. 2019, arXiv:1906.06305
Perez, S., Dunhill, A., Casassus, S., et al. 2015, ApJL, 811, L5
Pinte, C., Harries, T. J., Min, M., et al. 2009, A&A, 498, 967
Pinte, C., Ménard, F., Duchêne, G., et al. 2018a, A&A, 609, A47
Pinte, C., Ménard, F., Duchêne, G., & Bastien, P. 2006, A&A, 459, 797
Pinte, C., Price, D. J., Ménard, F., et al. 2018b, ApJL, 860, L13
Pinte, C., van der Plas, G., Ménard, F., et al. 2019, NatAs, 3, 109
Price, D. J., Cuello, N., Pinte, C., et al. 2018, MNRAS, 477, 1270
Riols, A., & Lesur, G. 2019, A&A, 625, A108
Stone, J. M., Skemer, A. J., Hinz, P. M., et al. 2018, AJ, 156, 286
Teague, R., Bae, J., & Bergin, E. A. 2019, Natur, 574, 378
Teague, R., Bae, J., Bergin, E. A., Birnstiel, T., & Foreman-Mackey, D. 2018a, ApJL, 860, L12
Teague, R., Bae, J., Birnstiel, T., & Bergin, E. A. 2018b, ApJ, 868, 113
van der Marel, N., Dong, R., di Francesco, J., Williams, J., & Tobin, J. 2019, ApJ, 872, 112
Vigan, A., Bonavita, M., Biller, B., et al. 2017, A&A, 603, A3
Zhang, K., Blake, G. A., & Bergin, E. A. 2015, ApJL, 806, L7
Zhang, S., Zhu, Z., Huang, J., et al. 2018, ApJL, 869, L47